Orbit Control Techniques for Space Debris Removal Missions Using Electric Propulsion

Mirko Leomanni,* Gianni Bianchini,† Andrea Garulli,‡ Antonio Giannitrapani,§ and Renato Quartullo¶
University of Siena, 53100 Siena, Italy

https://doi.org/10.2514/1.G004735

Electric propulsion is currently seen as a key enabling technology for space debris removal missions aimed at deorbiting multiple debris targets. This paper develops an autonomous onboard orbit control strategy tailored to these missions. The control problem is divided into four stages, involving a sequence of low-thrust orbital transfer and rendezvous maneuvers. A feedback control law is derived for each maneuvering stage, by exploiting Lyapunov-based and model predictive control techniques. The proposed design is able to account for mission-specific performance and safety requirements, while satisfying on–off constraints inherent to the propulsion technology. Simulation case studies of a multidebris removal mission demonstrate the effectiveness of the proposed control strategy, and support the viability of electric propulsion for such type of missions.

I. Introduction

AN IMPRESSIVE amount of space debris such as discarded rocket stages, defunct satellites, and small fragments generated by explosions is orbiting the Earth. The debris density in the low Earth orbit (LEO) regime is currently so high that there is a tangible threat of frequent collisions becoming a reality. Collision probability is likely to increase in the near future, due to the deployment of constellations of thousands of LEO satellites. Ultimately, a cascade of collisions between these objects would lead to an exponential growth of the number of debris fragments, which may jeopardize space activities [1–3]. Motivated by such concerns, major space agencies have identified active debris removal as an essential risk mitigation procedure [4–6].

Space debris removal missions are composed of different phases: a servicing spacecraft must first approach a target debris, bring it to a lower altitude orbit, and then, in case of a multitarget mission, repeat the whole process. Because of the large velocity changes (Δv) involved in this process, the design of these missions is subject to stringent constraints. In particular, the amount of debris objects that can be deorbited is heavily dependent on the specific impulse (i.e., the fuel efficiency) of the propulsion system. In this respect, electric propulsion (EP) is seen as a key technology for reducing propellant consumption, thus enabling the removal of multiple debris targets within a single mission. Whereas the design of chemical-propelled debris removal missions is quite consolidated in the literature (see, e.g., [7–9]), that of EP-based missions is still in its first stage of development. A feasibility study of such type of mission is presented in [10]. The analysis is focused on a series of debris captures, aimed at removing the objects with the highest impact probability. Different propulsion technologies are considered, among which Hall effect thrusters (HETs) are identified as one of the most promising options. This choice is motivated by the inherent simplicity of HETs with respect to other EP systems and by the much larger achievable payload mass (i.e., number of objects that can be deorbited) compared with chemical engines. Similar conclusions are reached by the analysis in [11,12]. The thruster control system design is not addressed in these preliminary studies, which point out the need for specific research in this direction.

The removal of multiple debris pieces using EP involves a sequence of low-thrust orbital transfers and rendezvous maneuvers. These pose important guidance and control challenges, in terms of both safety and autonomy. In this respect, feedback control systems represent an effective solution [13–15]. Among the relevant control techniques, Lyapunov-based methods have been widely investigated for orbital transfer problems, and found to provide near-time-optimal/near-fuel-optimal solutions (see, e.g., [16–19]). Model predictive control (MPC) has proven to be effective for rendezvous operations, due to its ability to optimize suitable performance indexes, while enforcing input and state constraints [20–24]. Unfortunately, in many of these works the thrust command is modeled as a continuous control signal. This is undesirable in EP applications, as many EP engines are operated at a fixed thrust level, in order to maximize the thruster specific impulse. Moreover, EP systems are usually shut down during eclipses, so as to meet the limitations on the power available on board. Thus, the required thrust command is discontinuous (see, e.g., [25,26]).

In this paper, a prototype debris removal mission driven by EP is studied from the orbit control perspective. A modular feedback control design is devised, which accounts for the following mission stages: orbit raising, phasing, terminal rendezvous, and deorbiting. A discontinuous Lyapunov-based control law is proposed for the orbit raising and deorbiting stages, together with a method to optimally tune the controller parameters. The phasing and terminal rendezvous stages are tackled by adopting an MPC approach. This allows one to tradeoff fuel consumption and state regulation performance, while enforcing thrust and collision avoidance constraints. In particular, on–off thrust constraints dictated by the EP technology are taken into account by formulating a mixed integer linear program (MILP). To limit the computational burden, a linear programming (LP) relaxation tailored to the thrusting configuration is devised. All the proposed feedback control laws take advantage of a novel parameterization of the relative motion, based on nonsingular orbital elements. A detailed control system analysis is performed on a nonlinear truth model including the main environmental perturbations affecting LEO satellites. The simulation results, besides validating the proposed control approach, allow one to assess the feasibility of EP-based debris removal missions, in terms of flight time and propellant consumption.

This paper is organized as follows: Section II illustrates the considered space debris removal mission, and Sec. III details the dynamic models used to describe the orbital motion of the spacecraft and the debris. Sections IV and V discuss the orbital transfer and rendezvous control strategies, respectively. Detailed simulation case

Received 24 July 2019; revision received 28 November 2019; accepted for publication 21 April 2020; published online 18 May 2020.

*Research Associate, Department of Information Engineering and Mathematics; leomanni@diism.unisi.it.
†Professor, Department of Information Engineering and Mathematics; giannibi@diism.unisi.it.
‡Professor, Department of Information Engineering and Mathematics; garulli@diism.unisi.it.
§Professor, Department of Information Engineering and Mathematics; giannitrapani@diism.unisi.it.
¶Ph.D. Student, Department of Information Engineering and Mathematics; quartullo@diism.unisi.it.

studies of the reference mission are presented in Sec. VI, and conclusions are drawn in Sec. VII.

II. Reference Mission

In this section, the space debris removal mission considered in this paper is presented. The most relevant features of the mission are described, including the spacecraft and propulsion system layout, as well as the maneuvering phases employed to achieve the mission objective.

A. Reference Coordinate Frames and Notation

In this paper, four coordinate frames are used. The first one is the Earth-centered inertial (ECI) frame. Its axes are denoted by X_{ECI}, Y_{ECI}, and Z_{ECI}. The fundamental plane is the Earth's equatorial plane. The X_{ECI} axis points to the vernal equinox, the Z_{ECI} axis points toward the North Pole, and the Y_{ECI} axis completes a right-handed triad. The second one is the equinoctial (EQW) frame, whose axes are denoted by the letters E, Q, and W. The E axis is in the orbital plane at an angle equal to the ascending node angle with respect to the line of nodes. The W axis is aligned with the angular momentum vector, and the Q axis completes a right-handed coordinate system. The third coordinate frame is a radial-transverse-normal (RTN) frame centered at the spacecraft. The R axis is aligned to the radius vector joining the Earth's center and the satellite. The N axis is in the same direction as the W axis of the Equinoctial frame. The T axis completes a right-handed triad and is collinear with the spacecraft velocity vector for circular orbits. The fourth coordinate frame is the so-called spacecraft body frame, whose axes X_b, Y_b, and Z_b are rigidly attached to the spacecraft bus.

B. Mission Design

The objective of the reference mission is to capture multiple debris pieces and release them into a much lower orbit. For safety reasons, the release orbit is located below the International Space Station. The focus is on the most debris-populated area in LEO (altitude range of 800–1000 km and inclination range of 75–100 deg). The considered approach amounts to performing a series of capture and deorbit maneuvers. In each maneuver, a single debris object is removed. Because the debris objects are distributed on a discrete number of narrow inclination bands, with many objects populating each band (see, e.g., [10]), it is envisaged that a specific mission will deal only with objects belonging to the same inclination band.

The considered mission scenario is consistent with those proposed in the literature for space debris removal with EP. In particular, a HET unit is considered as the primary actuation device. It is located on a side of the spacecraft and aligned to the direction Y_b of the body frame. Thrust vector steering is achieved via attitude control. HET engines are typically fired at a constant thrust level, in order to maximize the fuel efficiency (i.e., the specific impulse) and to simplify the power processing unit design. Accordingly, it is assumed that the HET is driven by on–off control commands. The propulsion system design is complemented by a set of 24 cold gas microthrusters (CGTs) organized in orthogonal triads centered at the bus vertices. These are operated in groups of four to provide decoupled control forces along the three basis vectors of the body frame, while minimizing the torque generated about the spacecraft center of mass. Thrusters pointing in opposite directions are never fired simultaneously. The debris capture device is mounted on the opposite side of the HET. It is assumed that such a device is able to establish a rigid connection between the spacecraft and the debris (e.g., robotic arm; see [27,28]). The spacecraft bus layout is illustrated in Fig. 1.

The satellite is released into an initial parking orbit by a launcher, and the mission is assumed to start subsequently. According to typical design standards, the mission is divided into four stages: orbit raising, phasing, terminal rendezvous, and deorbiting. These are detailed in the following.

1. *Orbit Raising*

The purpose of orbit raising is to transfer the spacecraft from the initial parking orbit to a higher-altitude orbit close to that of the debris. In particular, an orbit with the same orientation and an altitude slightly lower than that of the target debris is considered. This is referred to as a *phasing orbit*, as it is used in the phasing stage to acquire a suitable initial phase for terminal rendezvous. Orbit raising is performed by using the HET thruster alone, in order to achieve a high fuel efficiency.

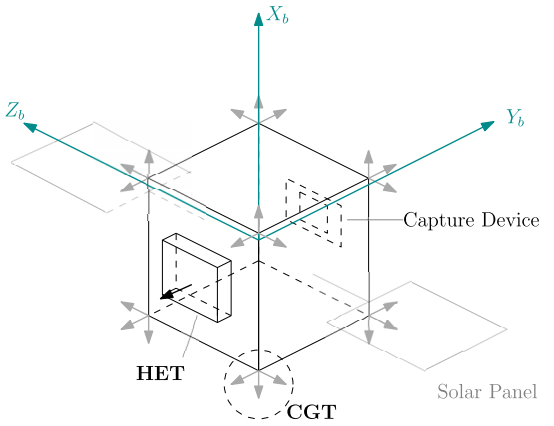

Fig. 1 Spacecraft layout, including the HET and CGT thrust vectors, as well as the capture device position with respect to the spacecraft body frame.

2. *Phasing*

Once the phasing orbit is reached, the HET is turned off and the spacecraft is left drifting until a good angular position for starting the phasing maneuver is acquired. The aim of the phasing maneuver consists in reaching a *holding point* situated a few kilometers ahead of the debris (in the direction of the orbital motion), along the debris orbit. In the phasing stage, the spacecraft body frame is kept aligned to the RTN frame. In particular, the Y_b axis points toward the positive T-axis direction. Both CGT firing and HET firing are allowed, in order to retain a high control authority. Nevertheless, it is preferable to use predominantly the HET, in order to consume as little propellant as possible. An important safety requirement in this stage is to avoid collisions with the debris.

3. *Terminal Rendezvous*

In the terminal rendezvous stage, starting from the holding point, the spacecraft is rotated so as to point the relative motion sensors and the capture device toward the debris object. The spacecraft attitude is then maintained fixed (with respect to the RTN frame) and the terminal rendezvous maneuver is performed. The aim of the maneuver is to reach a *capture point* a few meters ahead of the debris object, from which the capture device is activated. It is assumed that that target debris position is known and that the debris is not tumbling. Safety requirements in this stage are similar to those in the previous one.

4. *Deorbiting*

After the target debris has been captured, the HET is fired in order to drive the debris into a sufficiently low orbit, where it is released to reenter the Earth's atmosphere. To deorbit, the HET must be fired in the same direction as the orbital motion. For this reason, and considering the spacecraft layout in Fig. 1, the capture point is situated ahead of the target debris (i.e., in the positive V bar).

III. Orbital Dynamics

The dynamic models used to describe the orbital motion of the spacecraft and the debris are detailed hereafter.

A. Truth Model

The truth model adopted for simulation purposes includes the dynamics of the spacecraft and of the debris objects, as well as the spacecraft mass dynamics. The spacecraft dynamics are given by

$$\ddot{\boldsymbol{r}}^s = -\frac{\mu}{\|\boldsymbol{r}^s\|_2^3}\boldsymbol{r}^s + \boldsymbol{a}^s + \boldsymbol{u}_{\mathrm{ECI}} \tag{1}$$

where μ is the gravitational parameter, $\boldsymbol{r}^s$ indicates the spacecraft ECI position, $\boldsymbol{a}^s$ denotes the environmental disturbance acceleration, and $\boldsymbol{u}_{\mathrm{ECI}}$ is the ECI control acceleration. Clearly, $\boldsymbol{u}_{\mathrm{ECI}} = \boldsymbol{T}_{\mathrm{RTN}}^{\mathrm{ECI}}\boldsymbol{u}$, where $\boldsymbol{u}$ denotes the control acceleration expressed in the RTN frame, and $\boldsymbol{T}_{\mathrm{RTN}}^{\mathrm{ECI}}$ is the RTN-to-ECI direction cosine matrix. According to the propulsion system design in Fig. 1, one has

$$\boldsymbol{u} = \boldsymbol{u}_C + \boldsymbol{u}_H \tag{2}$$

where $\boldsymbol{u}_C$ and $\boldsymbol{u}_H$ are the RTN accelerations delivered by the CGTs and the HET, respectively. The variation in the spacecraft mass $m = m(t)$ is modeled by the equation

$$\dot{m} = -\frac{m}{g_0}\left(\frac{\|\boldsymbol{u}_C\|_1}{Isp_C} + \frac{\|\boldsymbol{u}_H\|_2}{Isp_H}\right) \tag{3}$$

where g_0 is the standard gravity, and Isp_C and Isp_H denote the specific impulses of the CGTs and the HET, respectively. Notice that in Eq. (3) the mass flow rate of CGTs is dictated by the 1-norm of $\boldsymbol{u}_C$, because the CGT system is employed only during phasing and rendezvous operations, in which the CGT units are aligned to the RTN axes (see Sec. II). In this case, $\|\boldsymbol{u}_C\|_1$ corresponds to the sum of the magnitudes of the thrust vectors of the single-CGT units. The debris dynamics are analogous to Eq. (1) with no control input, i.e.,

$$\ddot{\boldsymbol{r}}^d = -\frac{\mu}{\|\boldsymbol{r}^d\|_2^3}\boldsymbol{r}^d + \boldsymbol{a}^d \tag{4}$$

where $\boldsymbol{r}^d$ is the debris position and $\boldsymbol{a}^d$ denotes the environmental disturbance acceleration on the debris.

B. Control Design Model

A simplified dynamic model, including point-mass gravity and control accelerations, is considered for control synthesis. The satellite orbital motion is parameterized by the nonsingular orbital elements

$$\begin{aligned} x_1 &= \Omega + \omega + \psi \\ x_2 &= \sqrt{\mu/a^3} \\ x_3 &= e\cos(\Omega + \omega) \\ x_4 &= e\sin(\Omega + \omega) \\ x_5 &= \tan(i/2)\cos(\Omega) \\ x_6 &= \tan(i/2)\sin(\Omega) \end{aligned} \tag{5}$$

where x_1 is the true longitude, x_2 is the mean motion, (x_3, x_4) are the components of the eccentricity vector, (x_5, x_6) are the components of the ascending node vector, and a, e, i, Ω, ω, and ψ are the classical orbital elements (semimajor axis, eccentricity, inclination, RAAN, argument of periapsis, and true anomaly, respectively).

Let $\boldsymbol{x} = [x_1, \ldots, x_6]^T$. The dynamics of the controlled spacecraft can be expressed in terms of the elements (5) as follows:

$$\dot{\boldsymbol{x}} = \boldsymbol{f}(\boldsymbol{x}) + \boldsymbol{g}(\boldsymbol{x})\boldsymbol{u} \tag{6}$$

where the vector-valued function $\boldsymbol{f}(\boldsymbol{x})$ and the 6×3 input matrix $\boldsymbol{g}(\boldsymbol{x})$ are reported in [29], and $\boldsymbol{u} = [\,u_1 \quad u_2 \quad u_3\,]^T$, with u_1, u_2, and u_3 denoting the radial, transverse, and normal components of the control acceleration, expressed in the RTN frame centered at the spacecraft. System (6) is equivalent to Eq. (1) with $\boldsymbol{a}^s = \boldsymbol{0}$.

The dynamics of a debris object flying in a circular orbit turn out to be

$$\dot{\boldsymbol{x}}^d = [\,x_2^d \quad \boldsymbol{0}_{1\times 5}\,]^T \tag{7}$$

where the vector $\boldsymbol{x}^d$ contains the orbital elements of the debris. Notice that the elements $x_2^d, \ldots, x_6^d$ are constant along the (unperturbed) target orbit. The dynamic model (6) and (7) provides the baseline for the design of the control techniques presented in this paper.

C. Linearized Dynamics

To achieve the mission objective, the orbital elements x_j in Eq. (5) must be driven toward predefined reference values x_j^*, which depend the considered mission stage. In particular, the time-varying quantity $x_1^* = x_1^*(t)$ is defined as

$$x_1^*(t) = x_1^d(t) + \phi \tag{8}$$

where x_1^d is the debris true longitude and ϕ is a predefined angular offset. In the phasing stage, $\phi = \phi_{\mathrm{HP}}$, where ϕ_{HP} specifies the relative angle between the holding point and the debris. In the terminal rendezvous stage, $\phi = \phi_{\mathrm{CP}}$, where ϕ_{CP} indicates the capture point relative angle. The true longitude x_1 is not controlled in the orbit raising and deorbiting stages. The constant parameter x_2^* is used to specify the altitude of the phasing orbit in the orbit raising stage, as well as the orbital altitude at which a debris object is released in the deorbiting stage, while $x_2^* = x_2^d$ in the phasing and rendezvous stages. Moreover, $x_j^* = x_j^d$, $j = 3, \ldots, 6$, for all mission stages except for deorbiting, in which $x_3^*, \ldots, x_6^*$ specify the eccentricity and orientation of the release orbit.

The error between the actual and the reference orbital motion is parameterized in a way similar to [29] by the six-dimensional vector $\boldsymbol{y} = [y_1, \ldots, y_6]^T$, where

$$\begin{aligned} y_1 &= x_1 - x_1^* \\ y_2 &= \frac{x_2}{x_2^*} - 1 \\ \begin{bmatrix} y_3 \\ y_4 \end{bmatrix} &= \begin{bmatrix} \cos(x_1) & \sin(x_1) \\ \sin(x_1) & -\cos(x_1) \end{bmatrix}\begin{bmatrix} x_3 - x_3^* \\ x_4 - x_4^* \end{bmatrix} \\ \begin{bmatrix} y_5 \\ y_6 \end{bmatrix} &= \begin{bmatrix} \cos(x_1) & \sin(x_1) \\ \sin(x_1) & -\cos(x_1) \end{bmatrix}\begin{bmatrix} x_5 - x_5^* \\ x_6 - x_6^* \end{bmatrix} \end{aligned} \tag{9}$$

Moreover, the following time and input scalings are adopted

$$\mathrm{d}\lambda = x_2^*\mathrm{d}t, \qquad \boldsymbol{v} = \beta\boldsymbol{u} \tag{10}$$

where $\beta = (1/x_2^*(\mu x_2^*)^{1/3})$ is a positive constant, and $\boldsymbol{v} = [v_1, v_2, v_3]^T$. The scaled time variable λ will play the role of the integration variable in the model dynamics throughout the paper.

For the purpose of control design, the smooth mapping (9) is differentiated, taking into account Eqs. (6), (7), and (10), to give a nonlinear relative motion model. The latter is linearized about $\boldsymbol{y} = \boldsymbol{0}$ and $\boldsymbol{v} = \boldsymbol{0}$, assuming that the actual and the reference orbital elements are expressed with respect to the target EQW frame, and that the reference orbit is circular. The resulting linearized time-invariant dynamics read

$$\frac{\mathrm{d}\boldsymbol{y}}{\mathrm{d}\lambda} = \boldsymbol{A}\boldsymbol{y} + \boldsymbol{B}\boldsymbol{v} \tag{11}$$

where

$$\boldsymbol{A} = \begin{bmatrix} 0 & 1 & 2 & 0 & 0 & 0 \\ 0 & 0 & 0 & 0 & 0 & 0 \\ 0 & 0 & 0 & -1 & 0 & 0 \\ 0 & 0 & 1 & 0 & 0 & 0 \\ 0 & 0 & 0 & 0 & 0 & -1 \\ 0 & 0 & 0 & 0 & 1 & 0 \end{bmatrix}, \quad \boldsymbol{B} = \begin{bmatrix} 0 & 0 & 0 \\ 0 & -3 & 0 \\ 0 & 2 & 0 \\ 1 & 0 & 0 \\ 0 & 0 & 1/2 \\ 0 & 0 & 0 \end{bmatrix} \tag{12}$$

Similarly to what is observed in [29], model (11) holds for an arbitrary true longitude error. In fact, the matrices in Eq. (12) do not

change if the linearization point is taken as $\boldsymbol{y} = [\,\bar{y}_1 \quad \boldsymbol{0}_{1\times 5}\,]^T$, with $\bar{y}_1 \in [-\pi, \pi]$. In other words, the linearization (11) and (12) is valid on a ring-shaped region enclosing a circular reference orbit. For the problem at hand, linearization is justified by the fact that the considered debris objects lie in nearly circular LEO orbits, whose difference in radius is much smaller than the Earth radius (see, e.g., [10]).

IV. Orbital Transfer

The orbit raising and deorbiting maneuvers described in Sec. II consist in two orbital transfers. In this section, a feedback control scheme is devised for low-thrust orbital transfers between different LEO orbits.

A. Control Problem Formulation

During orbital transfers, only the error variables $y_2, \ldots, y_6$ need to be controlled (the true longitude error y_1 is left uncontrolled). To this aim, let us define the following subset of the error variables:

$$\boldsymbol{\xi} = [y_2, \ldots, y_6]^T \tag{13}$$

The linearized dynamics of the state vector $\boldsymbol{\xi}$ are given by the linear time-invariant model

$$\frac{\mathrm{d}\boldsymbol{\xi}}{\mathrm{d}\lambda} = \boldsymbol{A}_o\boldsymbol{\xi} + \boldsymbol{B}_o\boldsymbol{v} \tag{14}$$

where the matrices $\boldsymbol{A}_o$ and $\boldsymbol{B}_o$ are obtained from Eqs. (11–13) in a straightforward manner, because the first column of $\boldsymbol{A}$ is a zero vector.

According to the mission design in Sec. II, maneuvering is achieved by firing the HET and steering the thrust vector via attitude control. Then, $\boldsymbol{u}_C = \boldsymbol{0}$ and Eqs. (2) and (10) give $\boldsymbol{v} = \beta\boldsymbol{u}_H$. Hence, the actual HET thrust command is

$$F_H = m\|\boldsymbol{u}_H\|_2 = \frac{m}{\beta}\|\boldsymbol{v}\|_2 \tag{15}$$

while the azimuth and elevation angles of the thrust vector are reference commands fed to the attitude control system. The HET is operated in on–off mode, so that $F_H \in \{0, F_{\mathrm{MAX}}\}$, where F_{MAX} is a fixed thrust level. Consequently, the control input $\boldsymbol{v}$ must satisfy the constraint

$$\|\boldsymbol{v}\|_2 \in \left\{0, \frac{\beta F_{\mathrm{MAX}}}{m}\right\} \tag{16}$$

The considered orbital transfer problem consists of driving $\boldsymbol{\xi}$ toward a sufficiently small neighborhood of the origin, while satisfying the nonlinear constraint (16). A state-feedback control law of the form

$$\boldsymbol{v} = \boldsymbol{v}(\boldsymbol{\xi}) \tag{17}$$

will be derived to this purpose. Formally, our aim is to ensure that there exists a finite $\bar{\lambda} > 0$, such that

$$\boldsymbol{\xi}(\lambda) \in \mathcal{S}_\epsilon, \quad \forall\ \lambda \geq \bar{\lambda} \tag{18}$$

where $\mathcal{S}_\epsilon$ is a bounded set of states, from which the subsequent maneuver is initiated. More specifically, $\mathcal{S}_\epsilon$ is parameterized as

$$\mathcal{S}_\epsilon = \{\boldsymbol{\xi}\colon \|\boldsymbol{\xi}\|_2 \leq \epsilon\} \tag{19}$$

where $\epsilon > 0$ is a small parameter. Notice that Eq. (19), due to the eigenstructure of $\boldsymbol{A}_o$, is a positively invariant set for system (14) with $\boldsymbol{v} = \boldsymbol{0}$. In other words, if Eq. (18) is met at the scaled time instant $\bar{\lambda}$, one can guarantee that it is also met for all future $\lambda > \bar{\lambda}$, by simply applying $\boldsymbol{v} = \boldsymbol{0}$.

In the following a damping control scheme is proposed for the orbital transfer problem. Besides its simplicity, this technique has been shown to be effective in reducing significantly the transfer time [19,30].

B. Orbit Control Scheme

Herein, a feedback control law is presented for the linearized system (14), which satisfies the constraint (16) on the control input. First, let us observe that system (14) is controllable. Moreover, the unforced ($\boldsymbol{v} = \boldsymbol{0}$) system (14) admits the first integral

$$V(\boldsymbol{\xi}) = \frac{1}{2}\boldsymbol{\xi}^T\boldsymbol{K}\boldsymbol{\xi} \tag{20}$$

where

$$\boldsymbol{K} = \mathrm{diag}(k_1, k_2, k_2, k_3, k_3) \tag{21}$$

and k_1, k_2, and k_3 are positive constant scaling factors. In fact, due to the specific structure of $\boldsymbol{A}_o$ and $\boldsymbol{K}$, the derivative of Eq. (20) with respect to the scaled time λ is

$$\frac{\mathrm{d}V(\boldsymbol{\xi})}{\mathrm{d}\lambda} = \boldsymbol{\xi}^T\boldsymbol{K}\boldsymbol{A}_o\boldsymbol{\xi} + \boldsymbol{\xi}^T\boldsymbol{K}\boldsymbol{B}_o\boldsymbol{v} = \boldsymbol{\xi}^T\boldsymbol{K}\boldsymbol{B}_o\boldsymbol{v} \tag{22}$$

which vanishes when $\boldsymbol{v} = \boldsymbol{0}$. The existence of the first integral (20) allows one to construct a stabilizing controller of the form

$$\boldsymbol{v}(\boldsymbol{\xi}) = -\sigma(\boldsymbol{\xi})\left[\frac{\partial V(\boldsymbol{\xi})}{\partial \boldsymbol{\xi}}\boldsymbol{B}_o\right]^T = -\sigma(\boldsymbol{\xi})\boldsymbol{B}_o^T\boldsymbol{K}\boldsymbol{\xi} \tag{23}$$

where $\sigma(\boldsymbol{\xi})$ is any positive scalar function. Such an approach is commonly referred to as damping control.

To make Eq. (22) as negative as possible (with the aim of reducing the transfer time), while satisfying the constraint (16), $\sigma(\boldsymbol{\xi})$ in Eq. (23) is chosen as

$$\sigma(\boldsymbol{\xi}) = \begin{cases} 0 & \text{if } \|\boldsymbol{B}_o^T\boldsymbol{K}\boldsymbol{\xi}\|_2 = 0 \\ \dfrac{1}{\|\boldsymbol{B}_o^T\boldsymbol{K}\boldsymbol{\xi}\|_2}\dfrac{\beta F_{\mathrm{MAX}}}{m} & \text{otherwise} \end{cases} \tag{24}$$

The closed-loop system (3), (14), (23), and (24) is nonlinear and discontinuous, which complicates significantly the stability analysis. A possible way to simplify it is to assume a constant satellite mass m. This is reasonable because m changes very slowly when using EP. In this case, system (14), (23), and (24) turns out to be time invariant, and closed-loop stability can be proved by using the results in [30,31]. Specifically, by adopting Eq. (20) as a Lyapunov function, one can show that there exists an $\epsilon > 0$ such that all trajectories of Eqs. (14), (23), and (24) converge to the set $\mathcal{S}_\epsilon$ defined by Eq. (19); i.e., the closed-loop system is practically stable. Moreover, according to [30], the minimum value of ϵ for which Eq. (18) is satisfied decreases with decreasing values of $\beta F_{\mathrm{MAX}}/m$. Given that typically $\beta F_{\mathrm{MAX}}/m \ll 1$ for EP-based missions, convergence of the closed-loop trajectories toward a set that is small enough for practical applications is guaranteed. Eclipse effects are taken into account by enforcing $\boldsymbol{v} = \boldsymbol{0}$ in the eclipsed portion of the orbital path. This does not affect closed-loop stability, because the Lyapunov function (20) remains constant whenever $\boldsymbol{v} = \boldsymbol{0}$ [see Eq. (22)].

It should be noticed that scaling the gain matrix $\boldsymbol{K}$ in Eq. (21) by a positive constant factor does not change the control value provided by Eqs. (23) and (24). Hence, the entire parameter space (k_1, k_2, k_3) can be mapped to the positive orthant of a unit sphere. This corresponds to parameterizing the control gains as $k_1 = \cos(\alpha)\cos(\varphi)$, $k_2 = \sin(\alpha)\cos(\varphi)$, and $k_3 = \sin(\varphi)$, where $\alpha \in (0, \pi/2)$ and $\varphi \in (0, \pi/2)$. In this way, the optimization of the control policy can be conveniently cast as a two-dimensional search over the free parameters α and φ, for a given orbital transfer. Such procedure will

be illustrated in Sec. VI. It is also worth recalling that the considered damping control approach does not allow a specific phase angle to be targeted along the reference orbit. This control requirement is addressed in the rendezvous stage within an MPC framework, as detailed in the next section.

V. Orbital Rendezvous

Phasing and terminal rendezvous are configured as two distinct parts of the orbital rendezvous process. In this section, an MPC strategy tailored to low-thrust orbital rendezvous is proposed. A MILP formulation and a suitable relaxation exploiting the degrees of freedom provided by the thrusting system are presented.

A. Control Problem Formulation

In the rendezvous stage, the spacecraft body frame is aligned to the RTN frame. Maneuvering is achieved by firing a set of orthogonal CGT engines and an HET engine aligned with the T axis (see Sec. II). Thus, the control input $\boldsymbol{v}$ can be modeled as

$$\boldsymbol{v} = \boldsymbol{v}_C + [0 \quad sv_H \quad 0]^T \tag{25}$$

where $\boldsymbol{v}_C = \beta \boldsymbol{u}_C$, $v_H = \|\boldsymbol{v}_H\|_2$, and $\boldsymbol{v}_H = \beta \boldsymbol{u}_H$ [see Eqs. (2) and (10)], and the scalar s takes values $+1$ or -1, depending on the direction of the thrust generated by the HET. In particular, $s = 1$ during phasing operations, because in this stage the HET thrust vector points toward the positive T-axis direction, while $s = -1$ during terminal rendezvous, because in this stage the HET thrust vector points toward the negative T-axis direction. According to the mission design and to the propulsion system specifications, the control inputs in Eq. (25) must satisfy the constraints

$$\begin{aligned} \|\boldsymbol{v}_C\|_\infty &\le \frac{\beta T_{\mathrm{MAX}}}{m} \\ v_H &\in \left\{0, \frac{\beta F_{\mathrm{MAX}}}{m}\right\} \end{aligned} \tag{26}$$

where T_{MAX} and F_{MAX} denote the maximum thrust that can be delivered by the CGT system and the HET, respectively. The feasible input set for the CGT system is a box (modeled by the ∞-norm), because the CGT propulsion units are aligned with the RTN axes during rendezvous. As opposed to the HET input v_H, the CGT input $\boldsymbol{v}_C$ is assumed to be continuous. This assumption can be met either by using a set of proportional CGTs or by modulating the CGTs pulse width at a very high frequency, so as to obtain a continuous equivalent thrust. Notice that high-frequency thrust modulation is usually not feasible for HETs.

An important safety requirement is to guarantee collision-free trajectories. To this aim, we consider the following constraint:

$$c_1 \delta\theta + \frac{c_2}{a^*}\delta r \le d \tag{27}$$

where c_1, c_2, and d are constant parameters, $a^* = \mu^{1/3}(x_2^*)^{-(2/3)}$ is the target semimajor axis value, and $\delta\theta$ and δr denote, respectively, the angular and the radial separation between the spacecraft and the target debris, in a polar coordinate system. The boundary $c_1\delta\theta + c_2\delta r/a^* = d$ of Eq. (27) is defined so as to separate an admissible zone for the controlled spacecraft from another region containing the target debris (see, e.g., Fig. 2). Notice that $\delta\theta = y_1$, because the spacecraft and the debris orbits are coplanar during rendezvous, and

$$\delta r = a^*\left[\frac{1 - y_3^2 - y_4^2}{(1 + y_3)(1 + y_2)^{2/3}} - 1\right] \tag{28}$$

where we used Eq. (9), the orbit radius equation, and the fact that, for circular reference orbits, $y_3 = e\cos(\psi)$, $y_4 = e\sin(\psi)$. Linearizing Eq. (28) about $\boldsymbol{y} = \boldsymbol{0}$, we are able to approximate Eq. (27) as

$$c_1 y_1 - \frac{2c_2}{3} y_2 - c_2 y_3 \le d \tag{29}$$

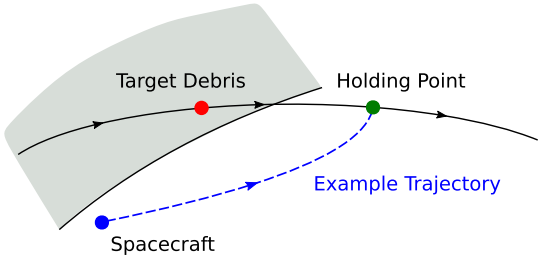

Fig. 2 Illustration of the state constraint (27), where the forbidden zone is grayed out.

According to the above linearization procedure, the constraint (29) is activated only when the spacecraft gets close to the debris. In the phasing stage, Eq. (29) is employed to guarantee that the spacecraft safely reaches the holding point; i.e., the resulting path is collision-free (see Fig. 2). In the terminal rendezvous stage, Eq. (29) is enforced to make the spacecraft follow a predefined glide slope toward the target, so as to ensure that the target remains within the field of view of the navigation instruments installed onboard the spacecraft [32]; see Fig. 8 in Sec. VI.

The rendezvous control problem consists of finding a state feedback control law $\boldsymbol{v} = \boldsymbol{v}(\boldsymbol{y})$, guaranteeing that

$$\lim_{\lambda\to\infty} \boldsymbol{y}(\lambda) = \boldsymbol{0} \tag{30}$$

while satisfying Eqs. (26) and (29). The control system must provide a compromise between fuel consumption and state regulation performance. On a given λ-interval of length Λ, the fuel consumption resulting from Eq. (3) is proportional to

$$\int_0^\Lambda \left\{\frac{m}{Isp_C}\|\boldsymbol{v}_C(\lambda)\|_1 + \frac{m}{Isp_H} v_H(\lambda)\right\} \mathrm{d}\lambda \tag{31}$$

The variation in the satellite mass m is typically very small during rendezvous operations. Hence, m can be safely modeled as a constant parameter, for control design purposes. As a measure of state regulation performance, we define the integral cost

$$\int_0^\Lambda \|\boldsymbol{Q}\boldsymbol{y}(\lambda)\|_1 \,\mathrm{d}\lambda \tag{32}$$

where $\boldsymbol{Q}$ is a full-rank weighting matrix. The adoption of the 1-norm allows one to formulate the control problem via linear programming techniques. Thus, the cost function to be minimized is

$$\int_0^\Lambda \{\|\boldsymbol{Q}\boldsymbol{y}(\lambda)\|_1 + \|\boldsymbol{v}_C(\lambda)\|_1 + r v_H(\lambda)\} \,\mathrm{d}\lambda \tag{33}$$

where $r = Isp_C/Isp_H$. Because the HET specific impulse is by far higher than the CGT one, one has that $r \ll 1$ in Eq. (33). In the following, an MPC strategy is devised for the rendezvous problem.

B. Rendezvous MPC Scheme

For the purpose of digital control design, system (11) and (12) is discretized with a sampling interval λ_s, by using a zero-order hold on the control input, resulting in the discrete-time model

$$\boldsymbol{y}(k+1) = \boldsymbol{A}_d \boldsymbol{y}(k) + \boldsymbol{B}_d \boldsymbol{v}(k) \tag{34}$$

The dimensional unit of λ_s is radians per sample, where 2π radians correspond to a full orbital period of the target debris object. Moreover, the cost function (33) is discretized as follows:

$$\sum_{k=0}^{N-1} \|\boldsymbol{Q}\boldsymbol{y}(k)\|_1 + \|\boldsymbol{v}_C(k)\|_1 + r v_H(k) \tag{35}$$

where $N = \Lambda/\lambda_s$.

To satisfy the control requirements (26), (29), and (30), while minimizing Eq. (35), the following optimization problem is formulated:

$$\begin{aligned}
&\min_{\hat{\boldsymbol{v}}_C,\hat{v}_H} \sum_{j=0}^{N-1} \|\boldsymbol{Q}\hat{\boldsymbol{y}}(j)\|_1 + \|\hat{\boldsymbol{v}}_C(j)\|_1 + r\hat{v}_H(j)\\
&\text{s.t. } \hat{\boldsymbol{y}}(j+1) = \boldsymbol{A}_d\hat{\boldsymbol{y}}(j) + \boldsymbol{B}_d\hat{\boldsymbol{v}}(j)\\
&\quad \hat{\boldsymbol{v}}(j) = \hat{\boldsymbol{v}}_C(j) + [0 \quad s\hat{v}_H(j) \quad 0]^T\\
&\quad \|\hat{\boldsymbol{v}}_C(j)\|_\infty \le \beta T_{\mathrm{MAX}}/m\\
&\quad \hat{v}_H(j) \in \{0, \beta F_{\mathrm{MAX}}/m\}\\
&\quad c_1\hat{y}_1(j) - \frac{2c_2}{3}\hat{y}_2(j) - c_2\hat{y}_3(j) \le d\\
&\quad \hat{\boldsymbol{y}}(0) = \boldsymbol{y}(k), \hat{\boldsymbol{y}}(N) = \boldsymbol{0}
\end{aligned} \tag{36}$$

where the decision variables are the control sequences

$$\hat{\boldsymbol{v}}_C = \{\hat{\boldsymbol{v}}_C(0), \ldots, \hat{\boldsymbol{v}}_C(N-1)\} \tag{37}$$

$$\hat{v}_H = \{\hat{v}_H(0), \ldots, \hat{v}_H(N-1)\} \tag{38}$$

The MPC strategy amounts to solving problem (36) at each discrete time step k and applying the control input

$$\boldsymbol{v}(k) = \hat{\boldsymbol{v}}(0) \tag{39}$$

to system (34), according to the receding horizon principle. Closed-loop exponential stability is guaranteed by the terminal constraint $\hat{\boldsymbol{y}}(N) = \boldsymbol{0}$ (see [33]).

Problem (36) can be cast as a MILP, in which N integer (binary) variables are used to model the control sequence (38). The computational complexity of this approach is known to scale badly with the length N of the prediction horizon. To mitigate this issue, a suitable relaxation is proposed, which exploits the flexibility provided by the spacecraft propulsion system layout. In particular, problem (36) is reformulated as

$$\begin{aligned}
&\min_{\hat{\boldsymbol{v}}_C,\hat{v}_H} \sum_{j=0}^{N-1} \|\boldsymbol{Q}\hat{\boldsymbol{y}}(j)\|_1 + \|\hat{\boldsymbol{v}}_C(j)\|_1 + r\hat{v}_H(j)\\
&\text{s.t. } \hat{\boldsymbol{y}}(j+1) = \boldsymbol{A}_d\hat{\boldsymbol{y}}(j) + \boldsymbol{B}_d\hat{\boldsymbol{v}}(j)\\
&\quad \hat{\boldsymbol{v}}(j) = \hat{\boldsymbol{v}}_C(j) + [0 \quad s\hat{v}_H(j) \quad 0]^T\\
&\quad \|\hat{\boldsymbol{v}}_C(j)\|_\infty \le \beta(T_{\mathrm{MAX}} - F_{\mathrm{MAX}})/m\\
&\quad 0 \le \hat{v}_H(j) \le \beta F_{\mathrm{MAX}}/m\\
&\quad c_1\hat{y}_1(j) - \frac{2c_2}{3}\hat{y}_2(j) - c_2\hat{y}_3(j) \le d\\
&\quad \hat{\boldsymbol{y}}(0) = \boldsymbol{y}(k), \hat{\boldsymbol{y}}(N) = \boldsymbol{0}
\end{aligned} \tag{40}$$

where the inequality $0 \le \hat{v}_H(j) \le \beta F_{\mathrm{MAX}}/m$ replaces the binary constraint $\hat{v}_H(j) \in \{0, \beta F_{\mathrm{MAX}}/m\}$, and $(T_{\mathrm{MAX}} - F_{\mathrm{MAX}}) > 0$ according to the characteristics of the propulsion devices ($F_{\mathrm{MAX}} \ll T_{\mathrm{MAX}}$). Problem (40) can be solved as a standard LP problem, for which computationally efficient tools are available. To generate control commands satisfying Eq. (26) from the solution to Eq. (40), the following control allocation scheme is proposed:

$$\begin{cases} \boldsymbol{v}_C(k) = \hat{\boldsymbol{v}}_C(0) \\ v_H(k) = \hat{v}_H(0) \end{cases} \quad \text{if } \hat{v}_H(0) \in \{0, \beta F_{\mathrm{MAX}}/m\}$$

$$\begin{cases} \boldsymbol{v}_C(k) = \hat{\boldsymbol{v}}_C(0) + [0 \;\; s\hat{v}_H(0) \;\; 0]^T \\ v_H(k) = 0 \end{cases} \quad \text{if } 0 < \hat{v}_H(0) < \beta F_{\mathrm{MAX}}/m \tag{41}$$

which means that the HET command is transferred to the CGT system whenever it does not comply with the on–off HET thrust constraints. This is possible because the upper bound on the CGT thrust command in Eq. (40) is slightly more conservative than the bound in Eq. (26). Clearly, the control input (25) resulting from Eqs. (40) and (41) is equal to that obtained by solving Eq. (40) and applying $\boldsymbol{v}(k) = \hat{\boldsymbol{v}}(0)$. Notice that the latter control is exponentially stabilizing, due to the terminal constraint $\hat{\boldsymbol{y}}(N) = \boldsymbol{0}$. Therefore, exponential stability holds also for Eqs. (40) and (41).

The proposed relaxation turns out to be useful for phasing operations, where a long prediction horizon N is required to adequately model the future system trajectory, being the initial relative distance between the spacecraft and the debris rather large. Instead, during terminal rendezvous, a much shorter horizon can be adopted, and the LP relaxation is not really necessary. In fact, if the prediction horizon is kept short enough, state-of-the-art MILP solvers can provide a solution to Eq. (36) in a reasonable amount of time.

VI. Simulation Case Studies

Hereafter, simulations of the reference mission described in Sec. II are presented. Two scenarios are considered. The first one involves the capture and deorbiting of two debris objects located in circular orbits with different altitudes. The second one considers the removal of a single debris element with an orbital eccentricity of 0.04 (this is a high value for debris objects in LEO). The most relevant initial orbital parameters of the spacecraft and the debris objects are reported in Tables 1 and 2 for the two scenarios. In this section, the orbit orientation parameters refer to the ECI frame (recall that these must be expressed with respect to the target EQW frame in the feedback control loop). The acronym RAAN denotes the right ascension of the ascending node.

The wet mass of the spacecraft is set to 100 kg, including 35 kg of propellant mass. The mass of each debris object is assumed to be equal to the spacecraft mass, i.e., 100 kg. The cross section of all bodies, which is used for environmental disturbance computation, is taken as 1 m^2. These parameters are consistent with the removal of debris elements such as nonoperational satellites, within a small satellite constellation. The maximum thrust levels deliverable by the HET and CGT systems are set to $F_{\mathrm{MAX}} = 15$ mN and $T_{\mathrm{MAX}} = 150$ mN, respectively, while their specific impulse is $Isp_H = 1200$ s and $Isp_C = 30$ s, according to the characteristics of such devices [34]. The spacecraft is assumed to be equipped with an energy storage unit (e.g., lithium batteries) able to operate the HET during eclipses. This feature is exploited for rendezvous maneuvers. Instead, during orbital transfers, the HET is turned off in correspondence of eclipses, so as to limit the number of battery charge/discharge cycles as well as the overall power draw of the propulsion system.

The mission has been simulated numerically by using the truth model (1–4) in combination with the control schemes derived in Secs. IV and V. The considered environmental perturbation models (see, e.g., [35]) are detailed in Table 3. For the purpose of control design, osculating orbital elements are converted into mean ones by

Table 1 Initial conditions of the spacecraft and of the two debris objects: scenario 1

Parameter	Spacecraft	Debris 1	Debris 2
Altitude, km	450	1000	950
Eccentricity	0	0	0
Inclination, deg	82	81	80
RAAN, deg	0	0	0

Table 2 Initial conditions of the spacecraft and of the debris object: scenario 2

Parameter	Spacecraft	Debris
Altitude, km	450	1000
Eccentricity	0	0.04
Inclination, deg	85	82
RAAN, deg	26.5	30

Table 3 Environmental perturbations included in the truth model

Source	Model
Earth's gravity	Earth Geopotential Model 1996 (EGM96), 9×9
Atmospheric drag	Naval Research Laboratory Mass Spectrometer and Incoherent Scatter Extended - 2000 (NRLMSISE-00), $F_{10.7} = 220$
Third body	Lunisolar point mass gravity
Solar pressure	Cannonball model with eclipses

using Brouwer's satellite theory [36]. In Sec. VI.A, each single stage of the capture and deorbiting process is discussed in detail, for the removal of debris 1 in Table 1. The complete mission analysis is reported in Sec. VI.B for both the considered scenarios.

A. Control System Analysis

1. *Orbit Raising*

The orbit raising objective is to drive the spacecraft toward the phasing orbit. This is done by using the control law (23) and (24). To optimally tune the controller, a two-dimensional search has been performed over the tuning parameters α and φ (see Sec. IV.B), by applying Eqs. (23) and (24) to the truth model (1–4) (taking into account eclipse effects), and evaluating the transfer time and fuel consumption for each combination of these parameters. The obtained results are shown in Fig. 3. Based on these data, the controller has been tuned with $\alpha = 10$ deg and $\varphi = 80$ deg. This choice results in minimizing both maneuver time and fuel consumption. In fact, it turns out that Eqs. (23) and (24) require the thruster to be always fired until maneuver completion, except during eclipses. Hence, the resulting fuel consumption is almost directly proportional to time, as it can be seen from Fig. 3.

The control law is implemented digitally by evaluating Eqs. (23) and (24) at discrete time samples and applying a zero-order hold to the control command $\boldsymbol{v}$. Constraints due to the minimum HET firing time and to the time needed for thrust vector steering are taken into account by adopting a sampling interval of 3 minutes. This is larger than both the minimum firing time and the time required to rotate the spacecraft by 180 deg about each of its body axes, assuming a maximum angular rate of 3 deg/s.

The evolution of the most relevant orbital parameters resulting from the simulation is reported in Fig. 4. The spacecraft orbital altitude successfully settles to the phasing orbit altitude, which is 20 km lower than that of the target debris. The overall transfer time is about 50 days, including 30 days for raising the altitude and about 20 days for eccentricity and inclination adjustments. The initial part of the thrust command profile F_H is depicted in Fig. 5. It can be seen that constraint (16) is satisfied, and that the thrust command does not exceed the maximum thrust F_{MAX} deliverable by the HET. Recall that the HET is shut down during eclipses, where $F_H = 0$. Most of the time the HET is fired along the tangential direction, so as to raise the orbital altitude. Near the end of the transfer, the HET is fired also in the radial and normal directions to compensate for eccentricity and inclination

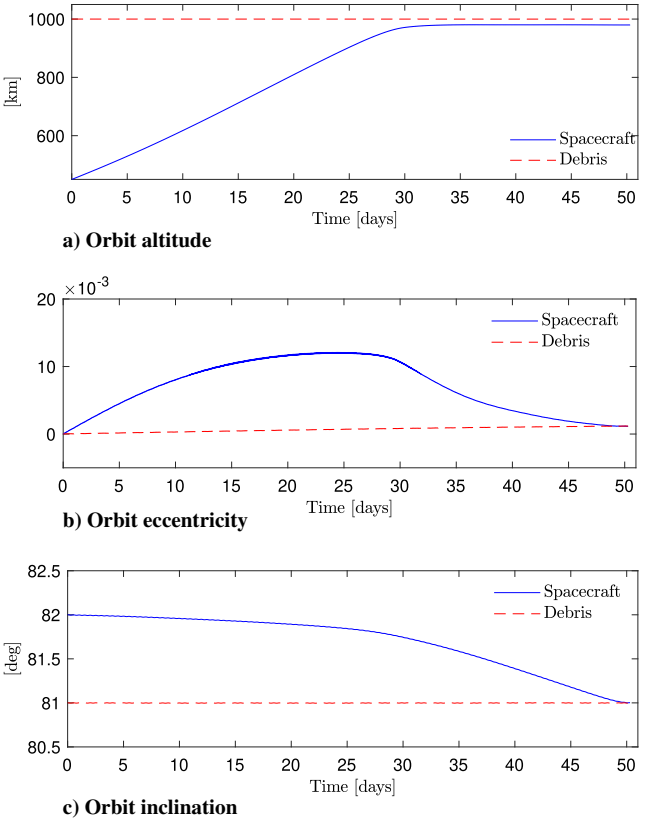

Fig. 4 Orbital parameters during orbit raising.

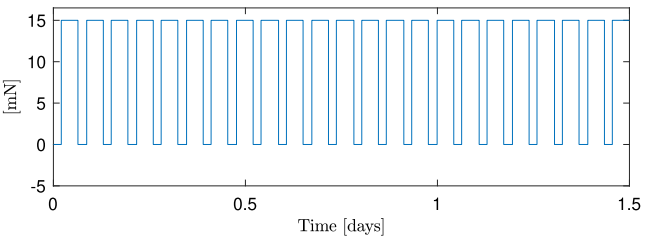

Fig. 5 HET command F_H on the time interval [0 1.5] days.

errors, respectively. The total Δv for the maneuver is 480 m/s, corresponding to a fuel consumption of 4 kg. In comparison, the Δv and fuel consumption predicted by the classical open-loop solution proposed by Edelbaum [37] amount to 350 m/s and 2.91 kg, respectively. The 37% higher Δv resulting from the application of Eqs. (23) and (24) can be attributed to the presence of eclipses, environmental perturbations, and RAAN adjustments, which are neglected in [37],

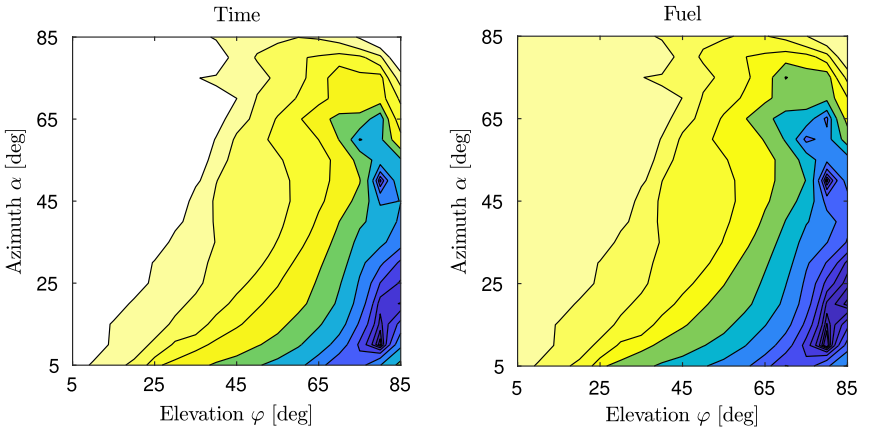

Fig. 3 Contour plot of the transfer time and fuel consumption obtained via a grid search over α and φ.

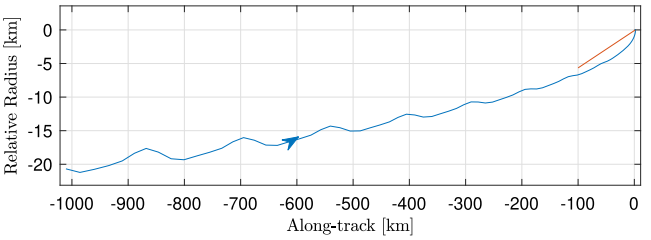

Fig. 6 Relative radius δr versus along-track displacement $a^*\delta\theta$ (blue), and state constraint boundary (red), during holding point acquisition; the state constraint is activated only when the along-track separation is smaller than 100 km.

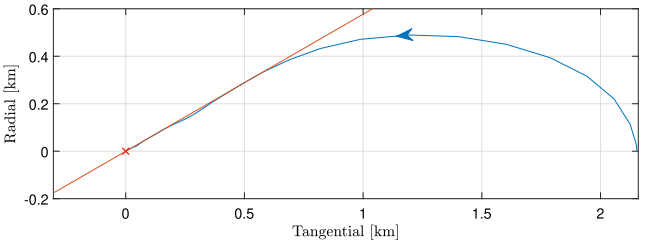

Fig. 8 Radial versus tangential separation (blue) and state constraint boundary (red), in the terminal rendezvous stage.

and to a certain degree of suboptimality of the nonlinear feedback design. In particular, the proposed feedback scheme employs radial thrusting to compensate for eclipse effects, while radial thrusting is not used in Edelbaum's solution.

2. *Phasing*

Once the phasing orbit is reached, the HET is turned off and the spacecraft is left coasting until a predefined longitude relative to the debris is acquired. A linear approximation of the relative longitude drift rate, which is valid for circular orbits, is given by the mean motion difference between the two bodies. By using this result, it follows that, for an initial relative radius of $\delta r = -20$ km, a worst-case estimate of the drift time (i.e., the time needed to change the relative longitude by 2π rad) is about 14 days. Such a delay is acceptable, in view of the overall duration of the mission.

Thrusting is initiated when the relative longitude reaches the value $x_1 - x_1^d = -0.138$ rad, with the objective of steering the spacecraft to the holding point defined by $\phi = \phi_{\text{HP}} = 2.7 \cdot 10^{-4}$ rad in Eq. (8), located 2 km ahead of the debris, in the along-track direction. This is achieved by using the control scheme (40) and (41), with $s = 1$. The sampling interval and the prediction horizon length are taken as $\lambda_s = \pi/4$ (corresponding to 8 samples per orbit) and $N = 110$, respectively. In this setting, the prediction horizon spans approximately 1 day. A trial-and-error procedure has been adopted to tune the weighting matrix $\boldsymbol{Q}$ in Eq. (36), so as to tradeoff fuel expenditure and state regulation performance, resulting in $\boldsymbol{Q} = 10^{-2} \cdot \text{diag}(0.05, 1, 1, 1, 7, 7)$.

Figure 6 depicts the evolution of the relative radius versus the along-track separation, together with the state constraint (29). The state constraint is activated only in the final part of the maneuver, so as to guarantee that the spacecraft passes at least 100 m below the debris while approaching the holding point (see also Fig. 2). Figure 7 depicts the HET thrust command, together with the tangential and normal components of the CGT command (the radial GCT component is omitted, as it is null). These satisfy the input constraints (26). Along-track maneuvering is achieved by firing mainly the HET, as expected. Moreover, it can be seen that the portion of the HET command provided by the LP relaxation (40) that does not satisfy Eq. (26) is transferred to the tangential CGT component by the control allocation scheme (41). The maneuver settling time amounts to approximately 1 day.

3. *Terminal Rendezvous*

The terminal rendezvous maneuver is initiated once $x_1 - x_1^d$ is approximately equal to ϕ_{HP}. The terminal rendezvous objective is to reach the capture point defined by $\phi = \phi_{\text{CP}} = 2 \cdot 10^{-7}$ rad in Eq. (8), which corresponds to positioning the spacecraft 1.5 m ahead of the debris for the considered orbit. This is achieved by using the mixed-integer MPC scheme (36–39), with $s = -1$. The sampling interval and the prediction horizon length are taken as $\lambda_s = \pi/16$

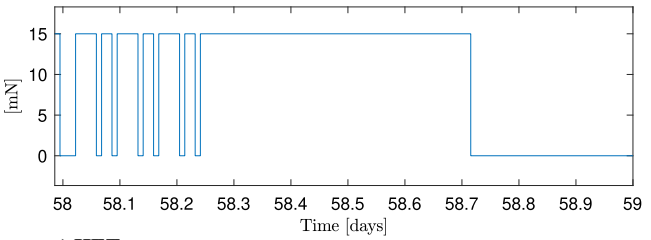

a) HET

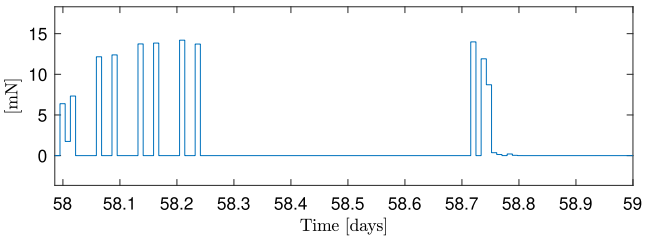

b) CGTs, tangential direction

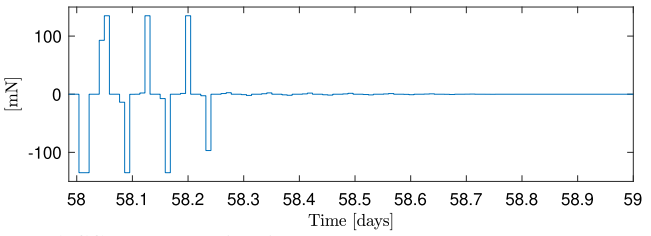

c) CGTs, normal direction

Fig. 7 Thrust profiles in the phasing stage.

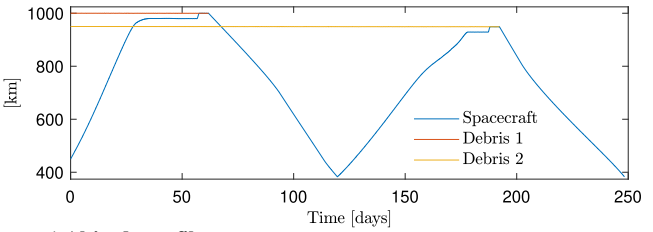

a) Altitude profile

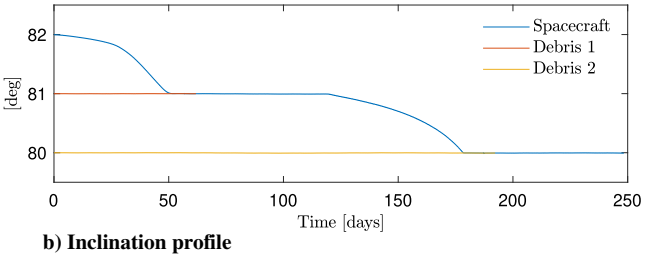

b) Inclination profile

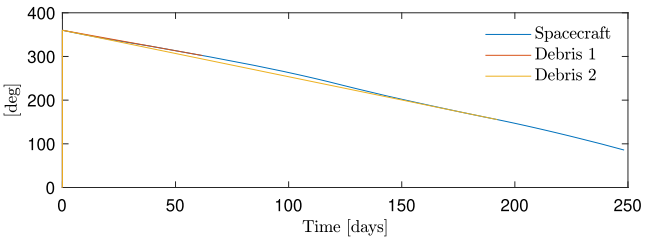

c) RAAN profile

Fig. 9 Evolution of the orbital parameters for scenario 1.

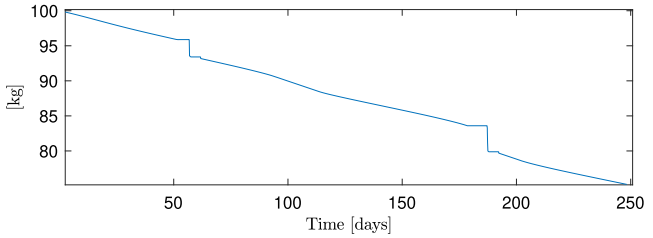

Fig. 10 Evolution of the spacecraft mass for scenario 1: the steep decrease on day 58 and day 190 is due to the activation of the CGT system.

(corresponding to 32 samples per orbit) and $N = 16$, respectively. A trial-and-error tuning of the controller led us to choose the same weighting matrix $\boldsymbol{Q}$ adopted for the phasing maneuver.

Figure 8 shows the evolution of the radial versus tangential displacement between the spacecraft and the debris, together with the state constraint (29). The constraint (29) ensures that the relative elevation angle, measured with respect to the local horizontal, does not exceed 30 deg. This value is compatible with the field of view of relative navigation instruments such as optical cameras. The maneuver settling time is approximately 2 h.

4. *Deorbiting*

The deorbiting maneuver is initiated as soon as the capture position is acquired and terminated when the debris object is released to naturally reenter the atmosphere (due to atmospheric drag forces). In this deorbiting case study, the debris is released at an altitude of 380 km, considering a high solar activity. Only the relative mean motion is controlled, by setting $k_2 = k_3 = 0$ in Eqs. (21), (23), and (24). The resulting control policy is such that the HET is always fired tangentially, in the direction of the orbital motion. This avoids thrust vector steering and thus a continuous reorientation of the spacecraft–debris pair. Simulation results indicate that the orbital eccentricity and ascending node vectors do not change significantly, despite that the gain on these elements is set to zero. Should these parameters experience large fluctuations, they can be actively controlled by enforcing $k_2 \neq 0$ and $k_3 \neq 0$, respectively.

B. Mission Analysis

Herein, the complete maneuvering profile is reported for the considered mission scenarios. Figure 9 shows the evolution of the altitude, inclination, and RAAN of the spacecraft, together with those of the two debris objects, for the scenario in Table 1. The secular RAAN drift is caused by the J_2 harmonic of the Earth's gravity field. The mission lasts 250 days and involves a propellant mass consumption of 24.77 kg (see Fig. 10), of which 18.31 kg is expended by HET and 6.46 kg by the CGT system. Based on these data and considering that the spacecraft carries 35 kg of propellant, we envisage that a small 100-kg-class spacecraft equipped with EP could remove up to three similarly sized debris objects, in a time interval of about 1 year. This matches the number of objects and the time span indicated in [10], in which a preliminary mission analysis is performed for a servicing spacecraft with similar propulsion specifications. In comparison, consider that small chemical-propelled spacecraft are expected to remove only a single debris piece per mission [10].

Simulation results for the scenario in Table 2 are depicted in Fig. 11. It can be seen that the debris object is successfully removed. In this case study, the release orbit altitude is set to 300 km. Moreover, the orbit is circularized in the deorbiting stage, so as to ensure that the servicing spacecraft does not fall below a minimum altitude of 200 km. Remarkably, the optimally tuned control law (23) and (24) takes advantage of atmospheric drag in order to reduce the deorbiting time. The overall fuel consumptions is 15.44 kg, including 11.31 kg for the HET and 4.13 kg for the CGT system, and the maneuver time is 162 days. These figures are fully compatible with the considered mission design and propulsion system specifications.

VII. Conclusions

A feedback control strategy has been devised for space debris removal missions driven by EP, taking into account maneuvering performance and safety requirements, as well as limitations dictated by the propulsion technology. The proposed design has been tested on two mission case studies, involving a sequence of low-thrust orbital transfer and rendezvous maneuvers. The obtained results show that the control scheme is able to achieve the mission objective, in a safe and autonomous manner. The fuel consumption and maneuver time have been also analyzed in detail, and are in line with previous concept studies. The proposed guidance and control techniques may contribute to bridge the gap between these studies and the implementation of electric-propulsion-based debris removal missions.

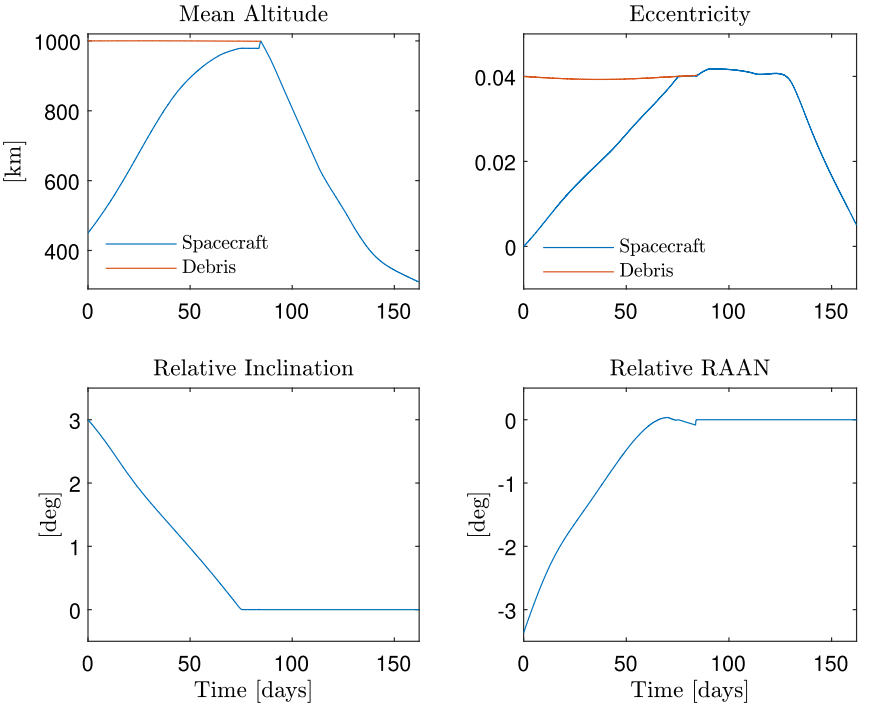

Fig. 11 Evolution of the orbital parameters for scenario 2.

References

[1] Kessler, D. J., and Cour-Palais, B. G., "Collision Frequency of Artificial Satellites: The Creation of a Debris Belt," *Journal of Geophysical Research: Space Physics*, Vol. 83, No. A6, 1978, pp. 2637–2646.
https://doi.org/10.1029/JA083iA06p02637

[2] Liou, J.-C., and Johnson, N. L., "Instability of the Present LEO Satellite Populations," *Advances in Space Research*, Vol. 41, No. 7, 2008, pp. 1046–1053.
https://doi.org/10.1016/j.asr.2007.04.081

[3] Kessler, D. J., Johnson, N. L., Liou, J., and Matney, M., "The Kessler Syndrome: Implications to Future Space Operations," *Advances in the Astronautical Sciences*, Vol. 137, No. 8, 2010, p. 2010.
https://doi.org/10.1.1.394.6767

[4] Liou, J.-C., "An Active Debris Removal Parametric Study for LEO Environment Remediation," *Advances in Space Research*, Vol. 47, No. 11, 2011, pp. 1865–1876.
https://doi.org/10.1016/j.asr.2011.02.003

[5] Wormnes, K., Le Letty, R., Summerer, L., Schonenborg, R., Dubois-Matra, O., Luraschi, E., Cropp, A., Krag, H., and Delaval, J., "ESA Technologies for Space Debris Remediation," *6th European Conference on Space Debris*, Vol. 1, ESA Communications ESTEC, Noordwijk, The Netherlands, 2013, pp. 1–8.

[6] Izzo, D., and Märtens, M., "The Kessler Run: On the Design of the GTOC9 Challenge," *Acta Futura*, Vol. 11, 2018, pp. 11–24.
https://doi.org/10.5281/zenodo.1139022

[7] Petropoulos, A., Grebow, D., Jones, D., Lantoine, G., Nicholas, A., Roa, J., Senent, J., Stuart, J., Arora, N., Pavlak, T., and Lam, T., "GTOC9: Methods and Results from the Jet Propulsion Laboratory Team," *Acta Futura*, Vol. 11, Jan. 2018, pp. 25–35.
https://doi.org/10.5281/zenodo.1139152

[8] Aslanov, V., and Yudintsev, V., "Dynamics of Large Space Debris Removal Using Tethered Space Tug," *Acta Astronautica*, Vol. 91, Oct. 2013, pp. 149–156.
https://doi.org/10.1016/j.actaastro.2013.05.020

[9] Jasper, L., and Schaub, H., "Input Shaped Large Thrust Maneuver with a Tethered Debris Object," *Acta Astronautica*, Vol. 96, March 2014, pp. 128–137.
https://doi.org/10.1016/j.actaastro.2013.11.005

[10] Ruggiero, A., Pergola, P., and Andrenucci, M., "Small Electric Propulsion Platform for Active Space Debris Removal," *IEEE Transactions on Plasma Science*, Vol. 43, No. 12, 2015, pp. 4200–4209.
https://doi.org/10.1109/TPS.2015.2491649

[11] Covello, F., "Application of Electrical Propulsion for an Active Debris Removal System: A System Engineering Approach," *Advances in Space Research*, Vol. 50, No. 7, 2012, pp. 918–931.
https://doi.org/10.1016/j.asr.2012.05.026

[12] Braun, V., Lüpken, A., Flegel, S., Gelhaus, J., Möckel, M., Kebschull, C., Wiedemann, C., and Vörsmann, P., "Active Debris Removal of Multiple Priority Targets," *Advances in Space Research*, Vol. 51, No. 9, 2013, pp. 1638–1648.
https://doi.org/10.1016/j.asr.2012.12.003

[13] Woffinden, D. C., and Geller, D. K., "Navigating the Road to Autonomous Orbital Rendezvous," *Journal of Spacecraft and Rockets*, Vol. 44, No. 4, 2007, pp. 898–909.
https://doi.org/10.2514/1.30734

[14] Breger, L. S., and How, J. P., "Safe Trajectories for Autonomous Rendezvous of Spacecraft," *Journal of Guidance, Control, and Dynamics*, Vol. 31, No. 5, 2008, pp. 1478–1489.
https://doi.org/10.2514/1.29590

[15] Starek, J. A., Açkmeşe, B., Nesnas, I. A., and Pavone, M., "Spacecraft Autonomy Challenges for Next-Generation Space Missions," *Advances in Control System Technology for Aerospace Applications*, Springer–Verlag, Berlin, 2016, pp. 1–48.
https://doi.org/10.1007/978-3-662-47694-9_1

[16] Ilgen, M. R., "Low Thrust OTV Guidance Using Lyapunov Optimal Feedback Control Techniques," *Advances in the Astronautical Sciences*, Vol. 85, Part 2, 1993, pp. 1527–1545.

[17] Chang, D. E., Chichka, D. F., and Marsden, J. E., "Lyapunov-Based Transfer Between Elliptic Keplerian Orbits," *Discrete and Continuous Dynamical Systems Series B*, Vol. 2, No. 1, 2002, pp. 57–67.
https://doi.org/10.3934/dcdsb.2002.2.57v

[18] Gurfil, P., "Control-Theoretic Analysis of Low-Thrust Orbital Transfer Using Orbital Elements," *Journal of Guidance, Control, and Dynamics*, Vol. 26, No. 6, 2003, pp. 979–983.
https://doi.org/10.2514/2.6926

[19] Petropoulos, A., "Low-Thrust Orbit Transfers Using Candidate Lyapunov Functions with a Mechanism for Coasting," *AIAA/AAS Astrodynamics Specialist Conference and Exhibit*, AIAA Paper 2004-5089, 2004.
https://doi.org/10.2514/6.2004-5089

[20] Richards, A., and How, J. P., "Robust Variable Horizon Model Predictive Control for Vehicle Maneuvering," *International Journal of Robust and Nonlinear Control*, Vol. 16, No. 7, 2006, pp. 333–351.
https://doi.org/10.1002/(ISSN)1099-1239

[21] Di Cairano, S., Park, H., and Kolmanovsky, I., "Model Predictive Control Approach for Guidance of Spacecraft Rendezvous and Proximity Maneuvering," *International Journal of Robust and Nonlinear Control*, Vol. 22, No. 12, 2012, pp. 1398–1427.
https://doi.org/10.1002/rnc.2827

[22] Leomanni, M., Rogers, E., and Gabriel, S. B., "Explicit Model Predictive Control Approach for Low-Thrust Spacecraft Proximity Operations," *Journal of Guidance, Control, and Dynamics*, Vol. 37, No. 6, 2014, pp. 1780–1790.
https://doi.org/10.2514/1.G000477

[23] Eren, U., Prach, A., Koçer, B. B., Raković, S. V., Kayacan, E., and Açkmeşe, B., "Model Predictive Control in Aerospace Systems: Current State and Opportunities," *Journal of Guidance, Control, and Dynamics*, Vol. 40, No. 7, 2017, pp. 1541–1566.
https://doi.org/10.2514/1.G002507

[24] Mammarella, M., Lorenzen, M., Capello, E., Park, H., Dabbene, F., Guglieri, G., Romano, M., and Allgöwer, F., "An Offline-Sampling SMPC Framework with Application to Autonomous Space Maneuvers," *IEEE Transactions on Control Systems Technology*, Vol. 28, No. 2, 2018, pp. 388–402.
https://doi.org/10.1109/TCST.2018.2879938

[25] Betts, J. T., "Optimal Low-Thrust Orbit Transfers with Eclipsing," *Optimal Control Applications and Methods*, Vol. 36, No. 2, 2015, pp. 218–240.
https://doi.org/10.1002/oca.v36.2

[26] Gazzino, C., Arzelier, D., Louembet, C., Cerri, L., Pittet, C., and Losa, D., "Long-Term Electric-Propulsion Geostationary Station-Keeping via Integer Programming," *Journal of Guidance, Control, and Dynamics*, Vol. 42, No. 5, 2019, pp. 976–991.
https://doi.org/10.2514/1.G003644

[27] Felicetti, L., Gasbarri, P., Pisculli, A., Sabatini, M., and Palmerini, G. B., "Design of Robotic Manipulators for Orbit Removal of Spent Launchers' Stages," *Acta Astronautica*, Vol. 119, Feb. 2016, pp. 118–130.
https://doi.org/10.1016/j.actaastro.2015.11.012

[28] Shan, M., Guo, J., and Gill, E., "Review and Comparison of Active Space Debris Capturing and Removal Methods," *Progress in Aerospace Sciences*, Vol. 80, Jan. 2016, pp. 18–32.
https://doi.org/10.1016/j.paerosci.2015.11.001

[29] Leomanni, M., Bianchini, G., Garulli, A., and Giannitrapani, A., "State Feedback Control in Equinoctial Variables for Orbit Phasing Applications," *Journal of Guidance, Control, and Dynamics*, Vol. 41, No. 8, 2018, pp. 1815–1822.
https://doi.org/10.2514/1.G003402

[30] Bombrun, A., and Pomet, J.-B., "Jurdjevic-Quinn Conditions and Discontinuous Bounded Damping Control," *Taming Heterogeneity and Complexity of Embedded Control*, Wiley, Hoboken, New Jersey, 2013, pp. 63–72, Chap. 5.
https://doi.org/10.1002/9780470612217.ch5

[31] Bacciotti, A., and Ceragioli, F., "Stability and Stabilization of Discontinuous Systems and Nonsmooth Lyapunov Functions," *ESAIM: Control, Optimisation and Calculus of Variations*, Vol. 4, 1999, pp. 361–376.
https://doi.org/10.1051/cocv:1999113

[32] Capello, E., Punta, E., Dabbene, F., Guglieri, G., and Tempo, R., "Sliding-Mode Control Strategies for Rendezvous and Docking Maneuvers," *Journal of Guidance, Control, and Dynamics*, Vol. 40, No. 6, 2017, pp. 1481–1487.
https://doi.org/10.2514/1.G001882

[33] Keerthi, S. A., and Gilbert, E. G., "Optimal Infinite-Horizon Feedback Laws for a General Class of Constrained Discrete-Time Systems: Stability and Moving-Horizon Approximations," *Journal of Optimization Theory and Applications*, Vol. 57, No. 2, 1988, pp. 265–293.
https://doi.org/10.1007/BF00938540

[34] Leomanni, M., Garulli, A., Giannitrapani, A., and Scortecci, F., "Propulsion Options for Very Low Earth Orbit Microsatellites," *Acta Astronautica*, Vol. 133, April 2017, pp. 444–454.
https://doi.org/10.1016/j.actaastro.2016.11.001

[35] Canuto, E., Novara, C., Carlucci, D., Montenegro, C. P., and Massotti, L., *Spacecraft Dynamics and Control: The Embedded Model Control Approach*, Butterworth-Heinemann, Oxford, 2018, pp. 129–236.
https://doi.org/10.1016/C2016-0-00420-5

[36] Brouwer, D., "Solution of the Problem of Artificial Satellite Theory Without Drag," *Astronomical Journal*, Vol. 64, Nov. 1959, pp. 378–397.
https://doi.org/10.1086/107958

[37] Edelbaum, T. N., "Propulsion Requirements for Controllable Satellites," *ARS Journal*, Vol. 31, No. 8, 1961, pp. 1079–1089.
https://doi.org/10.2514/8.5723